ADVANCED MATERIALS INTERFACES
Open Access
www.advmatinterfaces.de

Nanoengineering Scalephobic Surfaces for Liquid Cooling Enhancement

*Julian Schmid, Tobias Armstrong, Niklas Denz, Lars Heller, Lukas Hegner, Gabriel Schnoering, Jovo Vidic, and Thomas M. Schutzius**

Crystallization fouling, a process where mineral scales form on surfaces, is of broad importance in nature and technology, negatively impacting water treatment and electricity production. However, a rational methodology for designing materials with intrinsic resistance to scaling and scale adhesion remains elusive. Here, guided by nucleation physics, this work investigates the effect of coating composition and surface structure on the nucleation and growth mechanism of scale on metallic heat transfer surfaces nanoengineered by large-area techniques. This work observes that on hydrophilic nanostructured copper, despite its significantly enlarged surface area compared to smooth surfaces, scale formation is substantially suppressed leading to sustained, efficient cooling performance. This work reveals the mechanism through thermofluidic modeling coupled with in situ optical characterization and show that surface bubble formation through degassing is responsible for generating local hot spots enhancing supersaturation. This work then demonstrates a scalephobic nanostructured surface which reduces the accumulated surface scale mass 3.5× and maintains an 82% higher heat transfer coefficient compared to superhydrophobic surfaces with corresponding energy conversion savings. This work not only advances the understanding of fouling mechanisms but also holds promise for practical applications in industries reliant on efficient heat transfer processes.

1. Introduction

Scale formation on surfaces, such as the commonly encountered limescale, is pervasive in nature and technology, and can have extremely negative effects on energy conversion[1–3] and water treatment processes.[3–5] Despite substantial work, engineered surfaces with intrinsic scalephobic properties without the use of active methods like antiscalant additives remain elusive. This is because antiscalant surfaces are created today without sufficient reliance on an intricate but necessary science-base, of how interfacial thermofluidics, nucleation thermodynamics, and surface nanoengineering come together to control the onset of nucleation, growth, and adhesion of frequently encountered scaling salts like calcium carbonate and calcium sulfate. Such scaling salts have retrograde solubility in water and are common components of fouling deposits in industrial heat exchangers and membranes, which substantially inhibit heat transfer and flow performance. There is a growing need for a more sustainable approach[6] to address this issue with scalephobic surfaces that can inhibit the onset of nucleation or passively repel scale.[7–10]

Previous work on surface engineering has focused on developing scalephobic surfaces for flow cooling applications by modifying surface properties. A critical factor in designing these surfaces is the effect of surface roughness on nucleation, which remains inadequately understood. Some work suggests that rough surfaces can promote[11–14] scale formation by providing nucleation sites, while others report that increased roughness inhibits[13,15–17] nucleation or has negligible impact.[18] Beyond surface roughness, wettability[15,19,20] has been investigated as a parameter influencing scale formation. Techniques such as fluoropolymer deposition,[21,22] silane deposition,[20,23] and ion implantation[24] have been utilized to modify wettability, with increased surface energy correlating with increased fouling mass gain.[20] Additionally, superhydrophobic[25,26] and superhydrophilic surfaces,[10,27] including liquid-infused surfaces,[28,29] have been explored for their potential to minimize scale formation through inherent air[25,26] and liquid barrier layers.[10,27–32] Despite their promise, superhydrophobic and

J. Schmid, T. Armstrong, N. Denz, L. Heller, T. M. Schutzius
Laboratory for Multiphase Thermofluidics and Surface Nanoengineering
Department of Mechanical and Process Engineering
ETH Zurich
Sonneggstrasse 3, Zurich CH-8092, Switzerland
E-mail: tschutzius@berkeley.edu
L. Hegner, G. Schnoering, J. Vidic
Laboratory of Thermodynamics in Emerging Technologies
Department of Mechanical and Process Engineering
ETH Zurich
Sonneggstrasse 3, Zurich CH-8092, Switzerland
T. M. Schutzius
Department of Mechanical Engineering
University of California
Berkeley, CA 94720, USA

The ORCID identification number(s) for the author(s) of this article can be found under https://doi.org/10.1002/admi.202400383

DOI: 10.1002/admi.202400383

liquid-infused surfaces face significant challenges, primarily their propensity to degrade over time. Superhydrophobic surfaces can lose their air layer,[33] while liquid-infused surfaces can suffer from lubricant drainage.[34,35] In flow cooling applications, continuous fluid exposure exacerbates these issues, reducing the effectiveness and longevity of these surfaces. These surfaces were studied under various conditions, including pH variation,[15,36] which can effectively regulate solubilities, different levels of supersaturations,[20] and varying bulk and surface temperatures,[37,38] with increased temperature correlating with increased fouling.[38] The complex effects of flow velocity[16,39,40] and conditions on scale formation were examined, focusing on laminar[39–41] and turbulent flow.[16,42] To facilitate these investigations, continuous flow setups with localized heating were employed—as is done for many applications—complemented with in situ measured heat flux, surface temperature, and imaging[43] to study the scaling influence on heat transfer performance.[44]

Here, guided by nucleation, wettability, and heat transfer theories, we develop a methodology to study the nucleation and growth of calcium sulfate scale deposits and their negative influence on heat transfer in situ on engineered surfaces. We focus on the effects of chemical composition and surface nanostructure. Using a continuous flow fouling unit with microscopic in situ spatial resolution and heat transfer quantification under shear flow conditions, we reveal that hydrophobic surfaces result in substantially higher scale deposition than hydrophilic surfaces. This occurs because dissolved gases, like scaling salts, have retrograde solubility and form bubbles on the surface, creating local hot spots and enhancing scale deposition. By varying substrate nanostructure and composition to influence wettability, we quantify and demonstrate that hydrophilic surfaces prevent bubble formation, reduce residence time and bubble coverage, and reduce calcium sulfate deposition. We identify a fouling-enhancing mechanism caused by contact line effects of bubbles and rationalize it with a theoretical supersaturation model. By engineering a scalephobic nanostructured surface, we inhibit bubble formation, reduce residence time, and decrease scaling. We expect that the importance of bubble suppression through hydrophilic nanostructures on crystallization fouling without significantly altering the nucleation behavior of scale will guide the design of scalephobic surfaces.

2. Results

In order to study the influence of surface structure and chemical composition on crystallization fouling under flow conditions, we use a continuous flow fouling unit capable of characterizing simultaneously heat transfer performance and optical deposit formation on heated surfaces cooled by hard water (HW) (Figure S1, Supporting Information). **Figure 1a** shows the heated test section of the unit. At the beginning of each test, we heat the test surface to a surface temperature, T_S = 74–78 °C with an average $T_S \approx 76$ °C across all experiments, setting a constant electrical power input, P_{in}, without readjusting it throughout the experimental run. We cool the surface by circulating deionized (DI) water with bulk temperature, $T_B \approx 24$ °C, over it. Once the system thermally achieves a quasi-steady state, characterized by the constant T_S we switch over from pumping DI water to HW (saturated calcium sulfate solution) at a flow rate of $\dot{V} \approx 0.35$ L min^{-1}. We define this point as time-zero, $t = 0$ h. We then determine the temperature gradient in the copper rod, attached to the backside of the substrate, with distributed thermocouples (T_1 to T_5)—allowing us to quantify the average surface temperature, T_S, and heat flux q''—and we simultaneously image the surface deposition of calcium sulfate deposits, Figure 1b–d (Section S1, Supporting Information). The hydraulic diameter at the heated test section is d_h = 8.1 mm, resulting in a mean velocity of $\bar{u} \approx 0.05$ m s^{-1} and a Reynolds number of $Re = \rho \bar{u} d_h / \mu \approx 440$, where $\rho \approx 1000$ kg m^{-3} is the HW density and $\mu \approx 1$ mPa s is the fluid dynamic viscosity. We choose to work at this Reynolds number because fouling tends to be more pronounced under these conditions,[39] particularly in low-velocity regions of heat exchangers.[38] The supersaturation index of calcium sulfate in water can be defined as, $\sigma = \ln[(a_{Ca^{2+}})(a_{SO_4^{2-}})/K_{sp}]$, where $a_{Ca^{2+}}$ and $a_{SO_4^{2-}}$ are activities the calcium and sulfate ions and K_{sp} is the solubility product of the forming phase. The initial surface temperature of T_S = 74–78 °C, ensures a consistent supersaturation level of σ_{Gypsum} = 0.07–0.09 and $\sigma_{Anhydrate}$ = 0.50 (Tables S1 and S2, Supporting Information) at the start of the experiment for all tested surfaces. This consistency is crucial for effectively investigating the influence of surface characteristics on crystallization. The selected temperature range allows us to observe a fouling-induced increase of T_S by at least 20 °C, ensuring comprehensive data collection before reaching the nucleate boiling threshold and enabling us to conduct the experiment within a practical timeframe.

Throughout the experimental run the fouling deposits added thermal resistance to the system, resulting in an increase of T_S. Figure 1c,e shows image sequences, starting from $t = 0$ h, of the same heated electropolished hydrophilic copper at long and short time scales, respectively. We observe throughout the experiment the formation and growth of needle-shaped calcium sulfate crystals due to the local supersaturation of the solution at the heated surface. Initial deposits appear circular, interconnect over time, and eventually cover the entire observable area. We can link the visible observed crystallization process to T_S for a fixed P_{in}, Figure 1d. The growing interconnected fouling layer adds thermal resistance, due to its poor thermal conductivity (calcium sulfate: k = 0.8 – 2.2 W m^{-1} K^{-1}),[2] resulting in an increase in T_S, despite maintaining a constant P_{in}. In addition to calcium sulfate deposition, we observe the formation of surface bubbles that nucleate and adhere to the heated surfaces. We observe that the presence of bubbles substantially reduces the heat transfer and accelerates the formation of crystallites, Figure 1e. These bubbles either nucleate on the surface or grow from pre-existing gas cavities.[45] The nucleation or growth is driven by ≈1.5× lower solubility of dissolved natural gases in the locally heated solution than in the reservoir,[46] creating a supersaturation of the gas within the HW. The crystals form at the bubble-substrate contact line, resulting in a ring-shaped deposit after bubble departure. Previous work has shown similar effects.[47–50] We note that previous fouling studies attempted to prevent the formation of bubbles by degassing the solution,[43,48] a method that is impractical for large volumes of cooling water utilized in technical applications.

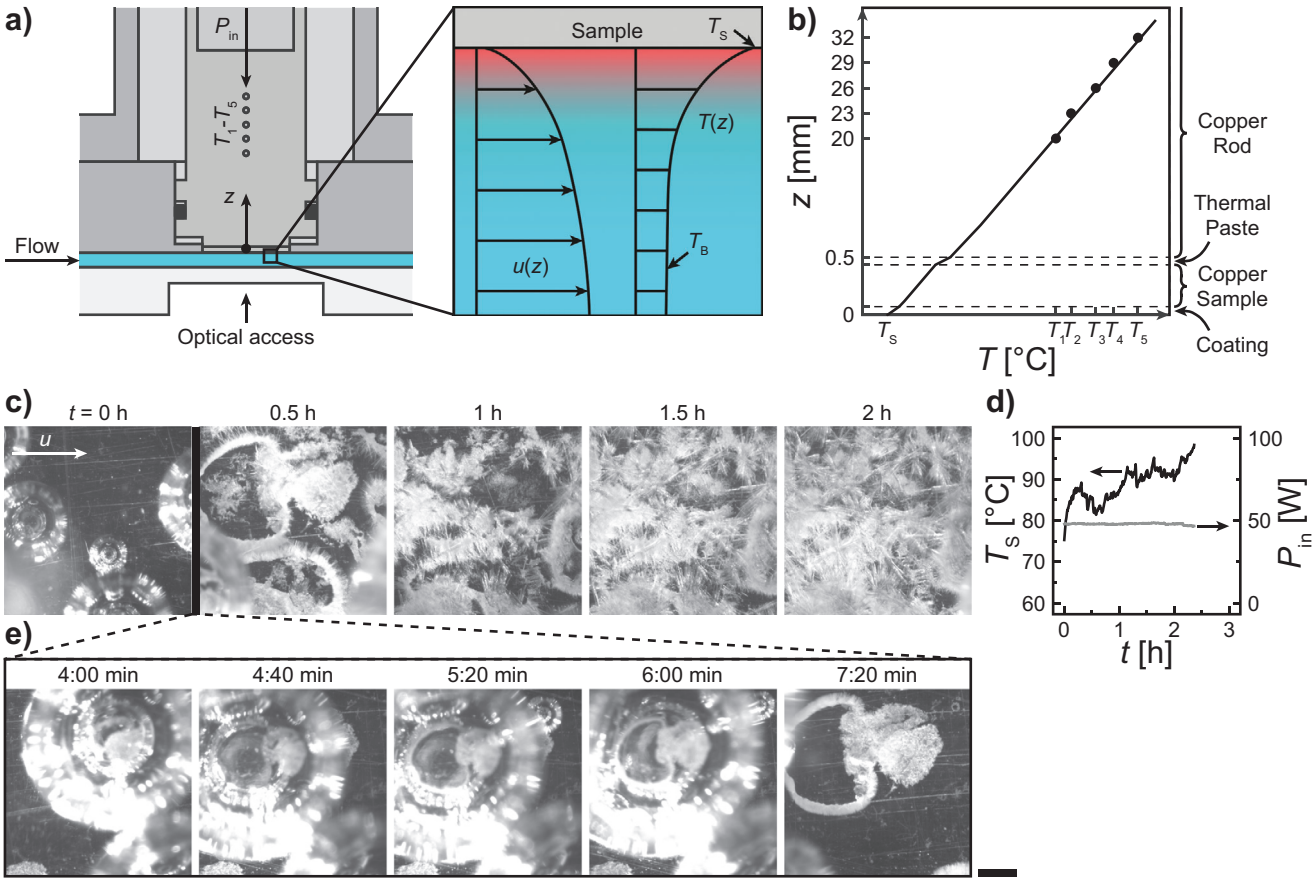

Figure 1. Experimental continuous flow fouling unit enables insight into crystallization fouling through localized heating by optical and heat transfer measurements. a) Schematic of a cut of the flow fouling unit at the heated surface: The sample surface (18 × 18 mm^2) is exposed to a fluidic channel (height $l = 5$ mm; width $w = 21.5$ mm; $Re = \rho \bar{u} d_h / \mu = 439$) with DI water during the experimental start-up procedure ($t < 0$ h), and saturated calcium sulfate solution during the observed crystallization fouling. The sample surface is heated from the backside by a heating cartridge in a copper rod with five thermocouple inlets ($T_1 - T_5$) at given distances, z, from the sample surface. Inset: Laminar velocity and temperature profiles at the sample surface. b) Extrapolation of measured temperatures in the copper block to obtain the sample surface temperature, accounting for the thermal paste and applied coatings. The temperature slope is proportional to the heat flux transferred into the fluid. c) Bottom-view image sequence of an uncoated electropolished copper sample (hydrophilic) showing the forming calcium sulfate deposits and their growth into an interconnected layer. Initial deposits appear circular. Fluid: HW d) Extrapolated surface temperature T_S and power input P_{in} through the heating cartridge over time t, showing increasing T_S at constant P_{in} until the experimental run stopped by reaching the stop criteria at a threshold temperature, $T_S = 98$ °C. e) Image sequence of the formation of the initial circular deposits showing how a formed degassing bubble gets pinned and calcium sulfate formation is initiated at the Solution-Surface-Bubble triple line before the grown bubble is large enough to be sheared off by the fluid flow. Fluid: HW. Scale bar: c), e) 200 µm.

To understand the underlying mechanisms of bubble formation, residence time, and the consequent impact on fouling it is desirable to separate the effects of bubble and scale formation. We reduce the complexity of the problem by performing experiments with DI water on surfaces exhibiting varying degrees of wettability. **Table 1** shows details on the nomenclature, treatment, average bubble coverage, bubble residence time and DI water heat transfer coefficients, h_{DI}, of the tested surfaces. **Table 2** shows the apparent advancing (index: a) and receding (index: r) contact angle measurements for DI water in air, θ^*_{DI}, air bubbles in DI water, ϕ*, and air bubbles in HW, ϕ^*_{HW}. For the superhydrophilic surface, the air bubble deviates from a spherical cap, and a contact angle cannot be measured (Figure S2, Supporting Information) **Figure 2**a–d shows image sequences of laminar DI water flow with constant T_B and T_S on various surface types.

We see that on the hydrophilic and superhydrophilic surfaces, the bubbles are more easily removed compared to the hydrophobic ones, leading to a reduced average bubble coverage (Table 1 and Experimental Section). Furthermore, the period from the first bubble detection to the first frame without the bubble is in the range of seconds to few minutes, indicating short bubble residence times (Table 1 and Experimental Section). In contrast, on hydrophobic and superhydrophobic surfaces, bubbles remain an extended period on the surface, showing deformation, deviating from the spherical cap shape. The presence of gas cavities on the (super)hydrophobic surfaces amplifies growth of bubbles from dissolved gases, leading to earlier bubble formation at even lower temperatures compared to the hydrophilic surface.[45] Figure 2e,f shows side-view and top-view schematics of the water-surface-bubble interaction with shear flow for a (super)hydrophilic and a (super)hydrophobic surface and the observed coalescence

Table 1. Nomenclature, wettability, bubble coverage, and DI water heat transfer coefficient of the tested surfaces. A detailed description of the contact angle measurements and the bubble coverage data analysis are described in the Experimental Section. We place a "–" sign if the value is too small to be measured.

Nomenclature	Material/Treatment	Average bubble coverage [%]	Bubble residence time [s]	h_{DI} [kW m^{-2} K^{-1}]
superhydrophilic	electropolished copper + chemical oxidation	2	≈ 3	1.59
hydrophilic	electropolished copper	72	≈ 65	1.42
hydrophobic	electropolished copper + iCVD (pPFDA)	94	≈ 220	1.07
superhydrophobic	electropolished copper + chemical oxidation + iCVD (pPFDA)	90	N/A	0.87

phenomena. While coalescing bubbles on hydrophilic surfaces form a spherical cap with a new contact line, the contact lines on hydrophobic surfaces are pinned, leading to a deformed coalesced bubble.

To explain the above results, we model the bubble removal dynamics by defining a hydrodynamic removal force, F_{hyd}, balanced with an adhesive force, F_{adh}, acting on the bubble parallel to the surface. This analysis accounts for the effects of bubble size, wettability, surface tension, and shear flow. The flipped, horizontal orientation of the setup (Figure S1, Supporting Information) is a conservative approach for bubble removal analysis as buoyancy acts perpendicular to the hydrodynamic force, effectively isolating the hydrodynamic force as the sole detaching mechanism. Based on the Reynolds number of the bubble, $Re_{bubble} = \frac{\rho_w \bar{v} H}{\mu} \approx 10^{-2}$, where ρ_w is the density of the water, $\bar{v}$ the mean velocity acting on the bubble of height H, and μ the dynamic viscosity of water, we can define F_{hyd} as the Stokes drag ($Re_{bubble} << 1$), acting on the bubble $F_{hyd} \approx 3\pi\mu\bar{v}Hf$, where f is a correction factor (1.7009), which accounts for the presence of the wall.[51] For the adhesive force F_{adh}, in our case surface tension forces, we can define the forces in horizontal direction as $F_{adh} \approx \frac{5}{4} a \gamma_{lv} \left(\frac{\pi\left(\phi_a^* - \phi_r^*\right)}{\pi^2 - \left(\phi_a^* - \phi_r^*\right)^2} \right) \left(\sin\phi_a^* + \sin\phi_r^*\right)$, where a is the contact radius of the bubble with radius, r, the liquid vapor surface energy,[52] γ_{lv}, and ϕ_a^* and ϕ_r^* are the advancing and receding contact angles of an air bubble in DI water on the surface, respectively.[53] We obtain values for ϕ_a^* and ϕ_r^* from our air bubble contact angle measurements in DI water (Experimental Section, Table 2 and Table S3, Supporting Information). Based on our in situ experiments, we can measure the projected diameter of the bubble d_m. For hydrophilic surfaces it is $r = d_m/2$ and for (super)hydrophobic surfaces it is $a = d_m/2$. Assuming a spherical cap we can define $H = r\,(1 - \cos(\phi^*))$ and $a = r\sin(\phi^*)$, where $\phi^* = (\phi_a^* - \phi_r^*)/2$ is the mean apparent contact angle. Therefore, the resulting force ratio can be described as

$$\frac{F_{hyd}}{F_{adh}} = Ca^* \frac{12\pi}{5\left(\frac{\pi\left(\phi_a^* - \phi_r^*\right)}{\pi^2 - \left(\phi_a^* - \phi_r^*\right)^2}\right)\left(\sin\phi_a^* + \sin\phi_r^*\right)} \quad (1)$$

where $Ca^* = \frac{H\mu\bar{v}f}{a\,\gamma_{lv}}$ is the modified capillary number, with $Ca^* < 10^{-5}$ for all surfaces. We find that the theoretical order of magnitude analysis for superhydrophilic, $\left(\frac{F_{hyd}}{F_{adh}}\right)_{phil} \approx 1.2$, and hydrophobic surfaces, $\left(\frac{F_{hyd}}{F_{adh}}\right)_{phob} \approx 3.7 \cdot 10^{-4}$, where $\frac{\left(F_{hyd}/F_{adh}\right)_{phil}}{\left(F_{hyd}/F_{adh}\right)_{phob}} \gg 1$, yields a good fit for the observed difference in bubble residence time and removal (Table 1).

This finding contrasts with prior fouling studies, which suggested that bubbles are more easily removed from hydrophobic surfaces.[48] Our observation and theoretical analysis better aligns with the findings in aerophobic literature.[54–60] In these studies, hydrophilic hydrogel[56–58] surfaces and, like our surface, nanostructured surfaces[59] with low contact angle hysteresis have demonstrated the ability to repel bubbles effectively. While we were unable to measure the contact angle hysteresis value for the superhydrophilic surface (Figure S2, Supporting Information), its excellent bubble repellency suggests that its hysteresis value should be comparable to those reported in the literature $\phi_a^* - \phi_r^* < 10°$. Furthermore, for the coalescence phenomena we observe for the (super)hydrophobic surfaces flow direction independent

Table 2. Air bubble contact angle measurements on the tested surfaces. We place a "–" sign if the value is too small to be measured. For the superhydrophilic surface, the air bubble deviated from a spherical cap, and a contact angle cannot be measured (N/A) (Figure S2, Supporting Information).

	DI water in air			Air in DI water			Air in HW		
Nomenclature	$180° - \theta^*_{r,DI}$ [°]	$180° - \theta^*_{a,DI}$ [°]	$\theta^*_{a,DI} - \theta^*_{r,DI}$ [°]	ϕ^*_a [°]	ϕ^*_r [°]	$\phi^*_a - \phi^*_r$ [°]	$\phi^*_{a,HW}$ [°]	$\phi^*_{r,HW}$ [°]	$\phi^*_{a,HW} - \phi^*_{r,HW}$ [°]
superhydrophilic	–	180	–	N/A	N/A	N/A	N/A	N/A	N/A
hydrophilic	164	93	71	166	95	71	163	102	61
hydrophobic	71	48	23	80	48	32	81	47	34
superhydrophobic	24	18	6	0	–	–	0	–	–

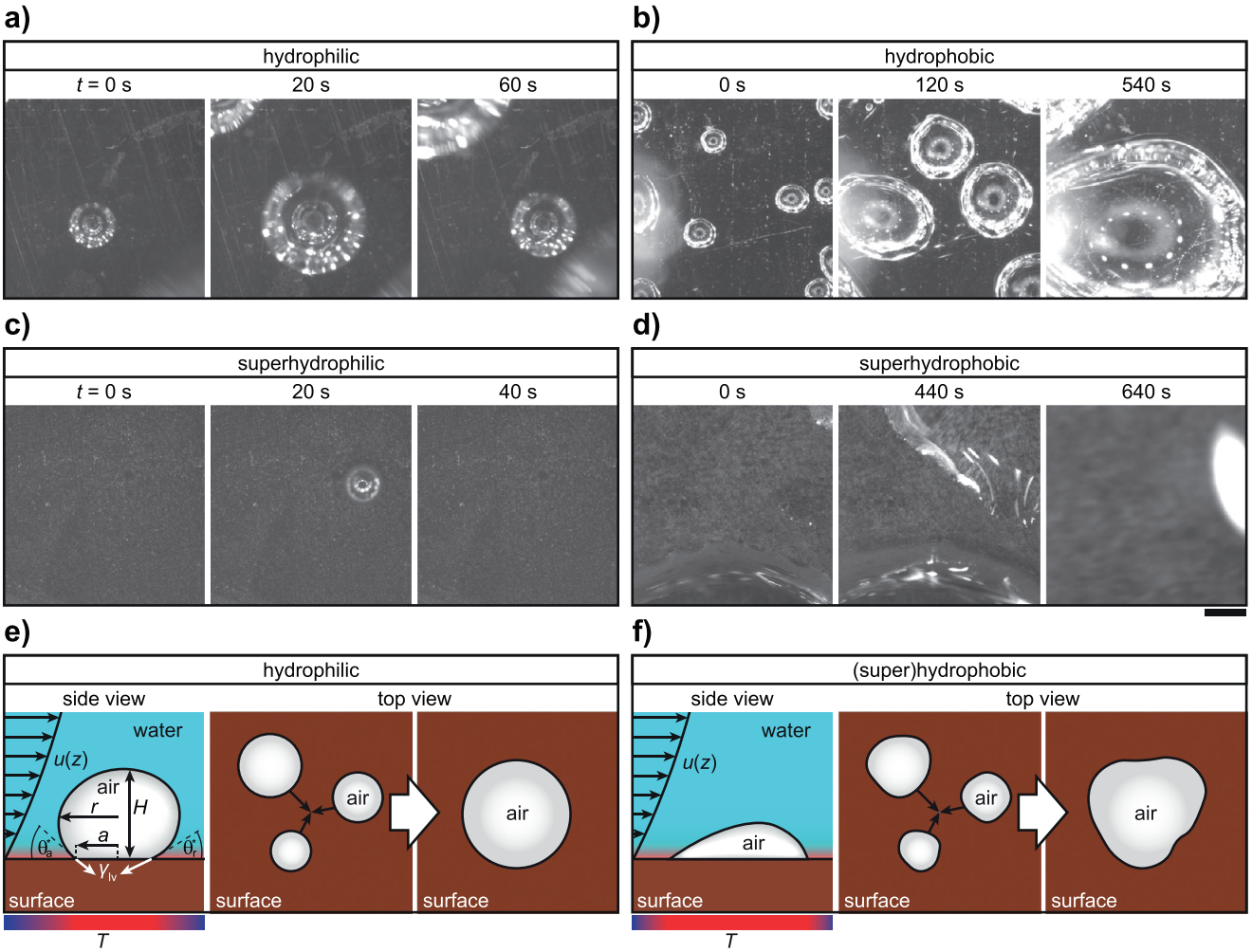

Figure 2. Surface bubble dynamics under shear-flow. Image sequences showing bubble growth on a) hydrophilic electropolished copper, h_{DI} = 1.42 kW (m^2 K)$^{-1}$, b) hydrophobic electropolished copper (pPFDA coating), h_{DI} = 1.07 kW (m^2 K)$^{-1}$, c) superhydrophilic copper oxide nanostructure (conformal pPFDA coating), h_{DI} = 1.59 kW (m^2 K)$^{-1}$, d) superhydrophobic copper oxide nanostructure (conformal pPFDA coating), h_{DI} = 0.87 kW (m^2 K)$^{-1}$. Fluid: DI water. Schematics showing the bubble shape and coalescence dynamics on e) hydrophilic, and f) (super) hydrophobic surfaces. Side-view schematics show the hydrophilic and hydrophobic nature of the substrates and the consequent influence on bubble contact radius and bubble height. The shear force acting on the water-bubble interface can be expressed as an effective hydrodynamic force F_{hyd} by accounting for the bubble geometry. Similarly, the adhesion force F_{adh} in horizontal direction holding the bubble on the substrate can be expressed in terms of surface tension forces. Scale bar: a–d) 200 μm.

movement of bubble-substrate contact lines which contribute to the unique behavior of bubbles on these surfaces and result in high overall average bubble coverages (see Table 1). The average bubble coverage substantially influences the surface's overall heat transfer coefficient, h,[61] which we can calculate using Newton's law of cooling: $h = q''/(T_S - T_B)$. Superhydrophilic surfaces demonstrate the highest h_{DI} = 1.59 kW (m^2 K)$^{-1}$, while superhydrophobic surfaces exhibit substantially lower h_{DI} = 0.87 kW (m^2 K)$^{-1}$ values (Figure S3, Supporting Information), consistent with findings from previous research[62] and corresponding to the surface type's respective bubble coverage for T_S after switching. The presence of bubbles covering the heat transfer area leads to an increase in local temperature beneath the bubble, which in turn reduces h. As a result, achieving the same T_S requires less P_{in}. Higher h values are crucial in heat transfer applications and a sought-after property apart from achieving scalephobicity.

Building upon the fundamental insights gained from studying the bubble behavior in water, we seek to understand the influence on surface properties and bubble formation on fouling. **Figure** 3a,c,e shows image sequences of bubble dynamics and fouling on heated surfaces being cooled with HW with constant T_B over various surface types heated to the same value of T_S(t = 0 h) (Movie S1, Supporting Information). The HW is saturated for T_B and supersaturated for T_S. We can define the fouling resistance as[1]

$$R_f(t) = \frac{1}{h(t)} - \frac{1}{h_0} \quad (2)$$

where $h(t)$ and h_0 are the overall heat transfer coefficients at t and t = 0 h, respectively. These coefficients are calculated using the temperature difference between the increasing surface

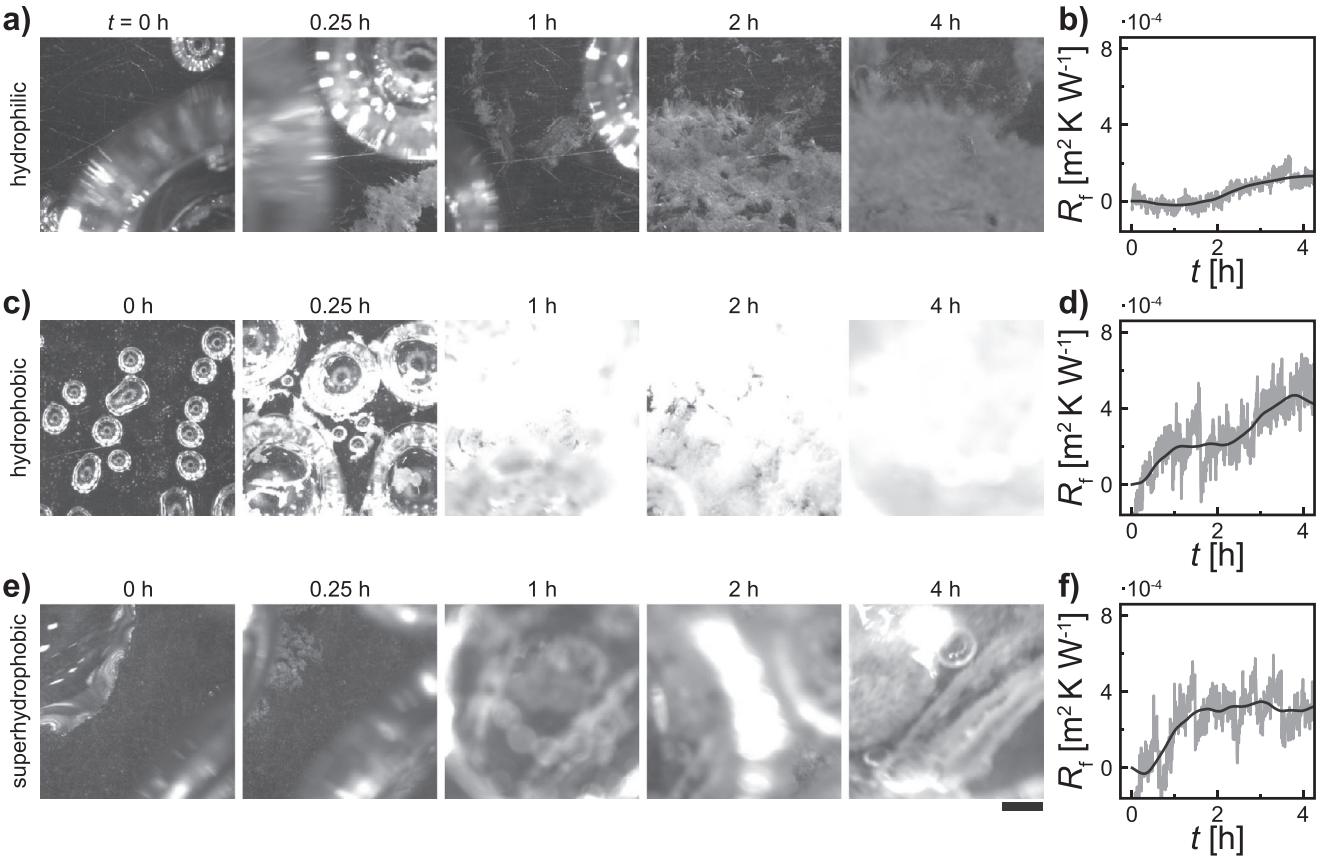

Figure 3. In situ characterization of crystallization fouling. Image sequences of crystallization fouling behavior on a) hydrophilic electropolished copper, c) hydrophobic electropolished copper with a pPFDA coating, e) superhydrophobic copper oxide nanostructure with a conforming pPFDA coating. Fluid: HW. b), d) and f) fouling resistance, R_f, versus t corresponding to the experimental tests shown in (a), (c), and (e), respectively. Grey and black lines represent raw and median filtered data, respectively. Scale bars: a), c), e) 200 µm.

temperature $T_S(t)$ due to fouling and the constant bulk temperature of the solution T_B. The fouling resistance serves as an indicator of the negative impact of the forming fouling layer on the overall heat transfer performance of the system. This includes the insulating effect of the fouling layer and potential variations in its porosity and thermal conductivity. As the fouling layer accumulates, the heat transfer efficiency between the surface and the cooling fluid decreases, resulting in decreased cooling performance. Figure 3b,d,f illustrates the evolution of fouling resistance R_f over t for the different surfaces.

On the hydrophilic surface, we observe bubble behavior similar to that observed in DI water flow (see Table 1). The bubbles cover a substantial portion of the observable hydrophilic surface. Despite their short residence time, we see the formation of crystals beneath the bubbles and around their contact line with the substrate. The median filtered R_f values during the initial 2 h stay below 0, indicating the initiation phase and roughness control phase[63]—with an increase in h caused by the disturbance of the viscous sublayer due to the increased roughness, of the crystals covering the surface—before entering the deposit growth phase.[1] It is important to note that detecting a change in R_f requires a minimum level of fouling mass gain. The primary fouling occurs between $t = 2$ and 4 h, during which the crystals intergrow and interconnect, resulting in an observable rise in R_f. On both hydrophobic and superhydrophobic surfaces, we observed an increased presence of bubbles similar to that observed in DI water flow (see Table 1). On the hydrophobic surface, bubbles detached at certain points, while on the superhydrophobic surface, bubbles cover the surface, for almost the entire experimental duration. Compared to the hydrophilic surface, we observe more fluctuation in the R_f values due to bubble influence, with a continuous median filtered R_f increase from the beginning of the experiment for both surfaces. Specifically, for the hydrophobic surface, this increase occurs throughout the full 4 h duration. However, for the superhydrophobic surface, we observe an asymptotic behavior after $t = 2$ h. This behavior is attributed to the insulation effect of the fouling layer, which reduces the temperature at the top of the layer in contact with HW. As a result, the temperatures to obtain supersaturation are not reached, and the growth stops.

Figure 4a,b illustrates experimentally and schematically how nucleation and growth at the bubble contact line occur for a superhydrophobic surface (Movie S2, Supporting Information). The contact line in Figure 4a moves not aligned with the flow direction, and we observe crystal formation in its vicinity. This movement relies on the presence of the hydrophilic nature of the crystals.[64,65] The dashed yellow reference line in all images marks the boundary between the clean and fouled surface areas at t = 80 s. Over time the crystals, particularly ≈200 µm from

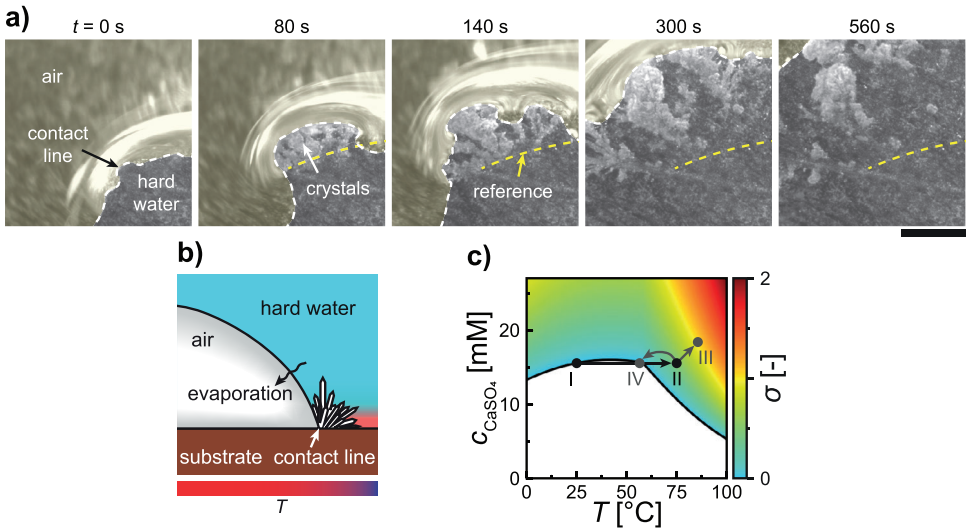

Figure 4. Fouling enhancement at the bubble contact line. a) Image sequence showing the motion of a bubble contact line and calcium sulfate deposition on a superhydrophobic substrate, flow direction left to right. Fluid: HW. The contact line advances in the same direction as the deposit growth (Movie S2, Supporting Information). b) Schematic side-view showing calcium sulfate deposition at the contact line. c) Plot supersaturation dependent on calcium sulfate concentration, c_{CaSO4}, and T of the HW. HW is initially saturated at room temperature as it enters the test section, $\sigma = 0$, at $T_B \approx 24$ °C (I). As the temperature increases, the water becomes supersaturated for calcium sulfate (II). For surfaces with high bubble residence time and high average bubble coverage (see Table 1), the bubble insulates the heat transfer surface, causing a locally increased HW temperature at the contact line, provides a route for vaporization, boosting supersaturation further (III). With increasing distance from the contact line, the temperature, hence supersaturation, decreases (IV). Scale bar, a) 200 µm.

the contact line, begin to dissolve, indicating undersaturation. In cases where bubbles persist for extended periods without detaching (see Figure 2, Table 1), the low thermal conductivity of the air leads to an insulating effect creating a non-uniform temperature distribution with high temperatures beneath the bubbles.[50] These hot spots are expected to increase the supersaturation near the contact line, σ, enhancing deposition probability. Furthermore, the presence of the bubble interface facilitates water vaporization, additionally leading to a scenario where there is a further local increase in σ due to water depletion as a result of this vaporization. With increased distance to the contact line the temperature decreases below T_S, and can cause an undersaturation resulting in the observed dissolution at $t = 300$ s. By reducing the presence of surface bubbles, thereby minimizing hot spots, more heat can be effectively transferred with a narrower temperature spread around T_S, resulting in decreased contact line temperatures.

Figure 4c illustrate the supersaturation diagram of $CaSO_4$, showing its dependence on both solute concentration, c_{CaSO_4}, and temperature, T, beyond the solid solubility line. In our experiments, we ensured the solution was saturated (Experimental Section) in both the reservoir and bulk flow. When no bubbles are present, the HW becomes supersaturated due to an increase in T_S. In cases where surface bubbles form, the supersaturation increases further due to their promotion of hot spots, and vaporization, depleting water and increasing c_{CaSO_4}. Conversely, as the distance from the contact line increases, the solution remains at the same concentration but experiences cooler temperatures, which can even drop below the solubility line. The increase in supersaturation due to temperature and evaporation, as well as the temperature itself, reduces the free energy barrier to nucleation, $\Delta G_{Het} = g\Delta G_{Hom} \propto 1/T^2\sigma^2$, where $g \in [0, 1]$ is the geometric factor accounting for heterogenous nucleation.[5] Moreover, it exponentially enhances the nucleation rate of calcium sulfate, which scales as, $J = A\exp(-\Delta G_{Het}/kT) \propto \exp(-1/T^3\sigma^2)$, where A is a kinetic pre-factor, and k is the Boltzmann constant. In addition to the influences in σ and T, the geometric factor g decreases for nucleation at the contact line.[66] So, while preventing surface bubbles appears to be a clear strategy toward enhancing scale-phobicity, the effect of surface composition and structure on ΔG for calcium sulfate is not clear. Due to the increase in surface area,[67] and nanoscale surface pits potentially locally reducing g and therefore ΔG,[68] one would expect that the nucleation rate should increase, enhancing fouling. Building upon the fundamental insights gained from studying the contact line behavior, we seek to rationally design surfaces with inherent surface bubble prevention, while not decreasing the nucleation barrier for $CaSO_4$.

Our theoretical analysis highlights the importance of increasing F_{hyd}/F_{adh} (see Equation 1), which means minimizing F_{adh} and maximizing F_{hyd}. To achieve this one can manipulate ϕ_a^* and ϕ_r^* of the surface through engineering the surface composition and structure at length scales smaller than the bubbles. To simultaneously minimize F_{adh} and maximize F_{hyd}, the hysteresis $\phi_a^* - \phi_r^*$ (Table 2) has to be reduced potentially to a value of $\phi_a^* - \phi_r^* < 10°$ in alignment with aerophobic literature,[56–60] while the absolute values of ϕ_a^* and ϕ_r^* have to be maximized, which results in superhydrophilicity. Additionally, the nanostructure enhances the bubble mobility, avoiding pinning of the contact line.[54] To see whether this approach works and not substantially decreases the nucleation barrier for $CaSO_4$, we perform fouling runs on superhydrophilic surfaces.

Figure 5a,b shows an image sequence and the corresponding R_f evolution of a superhydrophilic nanostructured surface,

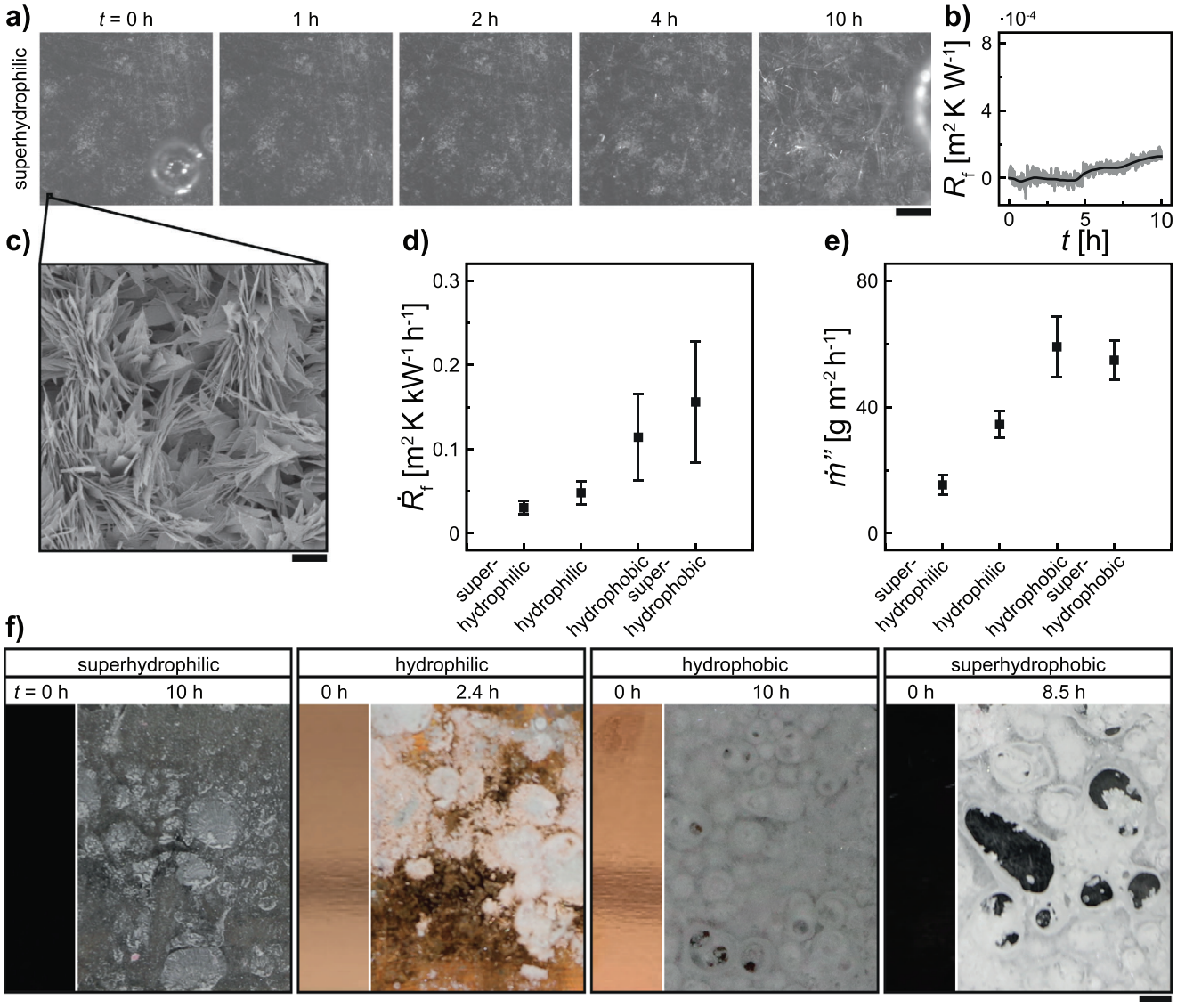

Figure 5. Rational design of scalephobic surfaces through bubble suppression and mechanistic insights of crystallization fouling. a) Image sequences of bubble suppression and crystallization fouling behavior on superhydrophilic copper oxide nanostructure and the corresponding fouling resistance evolution, b) Fluid: HW. c) Micrograph of copper oxide nanostructure d). Comparison of fouling resistance rates $\dot{R}_f$ d) and ex situ time-area averaged mass gain e) for the tested substrates on N ≥ 3 independent samples. Ex situ images of the surfaces before and after crystallization fouling. Scale bars: a) 200 µm, c) 2 µm, f) 2 mm.

respectively, with the micrograph of the nanostructure in Figure 5c (Figure S4, Supporting Information). We obtain the fouling resistance evolution R_f from measurements subjected to the same conditions as those in the experiments presented in Figure 3 but extended to 10 h experiment time (Movie S1, Supporting Information). The initial 4 h of the experiment show solely single crystals, with minimal intergrowth or formation of a continuous fouling layer, resulting in a roughness control phase with stable R_f values. Following this initial period, we observe a gradual increase in visual fouling and R_f values until the end of the 10 h experiment, without reaching the stop criteria (Experimental Section). Despite this, we still do not observe an intergrown fouling layer, and the fouling is less dense compared to the other three surfaces. This observation indicates that the prevention of bubbles on the superhydrophilic surface is crucial and there is no substantially decreased nucleation barrier for $CaSO_4$ countering this effect.

Once the deposit growth phase starts, the increase in R_f can be approximated linearly by an average fouling resistance rate $\dot{R}_f$. Figure 5d depicts the average $\dot{R}_f$ for the four different surfaces. The superhydrophobic surface exhibits the highest $\dot{R}_f$, with a general decreasing trend as hydrophilicity increases, resulting in a ≈ 5× decrease for the superhydrophilic surface. This trend is similarly for the ex situ measured, area and time averaged mass gain in Figure 5e, indicating a ≈3.5× improvement in performance of the superhydrophilic compared to the superhydrophobic surface. In case of evaluating the experiments after 2 h, the performance increase is even higher for the superhydrophilic

surface, considering that the (super)hydrophobic surface fouling occurs within this period (see Figure 3d,f), while superhydrophilic surfaces have not enter the deposit growth phase.

Figure 5f shows ex situ images before and after fouling for each surface type. After the experiment, the superhydrophilic surface exhibits nearly complete coverage by white crystals, although dense deposit structures are only observed in a few spots. Partially unfouled regions were observed on the hydrophilic sample due to the stop criteria $T_S > 98$ °C being met before the entire surface was covered. This observation highlights that dense deposits can elevate T_S to meet the stop criteria, particularly on hydrophilic surfaces attributed to their higher P_{in} compared to the (super)hydrophobic surfaces. On the hydrophobic surface, we observed crater formation, indicating that the bubbles remained on the surface for an extended duration. On the superhydrophobic surface, we can observe an increase in the size of these bubble craters and identify areas where the bubbles remained pinned throughout the entire experiment, with no fouling occurring beneath them. Such large bubbles were only present for an extended duration on the superhydrophobic surface, consistent with the findings for DI water (see Figure 2d, Table 1).

3. Conclusion & Discussion

We have developed, guided by nucleation, wettability, and heat transfer theories, a methodology, using a continuous flow fouling unit, to study nucleation and growth of calcium sulfate scale deposits in situ on engineered heat transfer surfaces. The methodology offers the necessary microscopic spatial resolution paired with heat transfer quantification to study fouling which can improve the approach to develop scalephobic surfaces. By providing insights at the microscale, where fouling initiates and where sustainable prevention efforts are targeted, the work reveals the intricate and negative effects of bubbles on heat transfer and scaling. Furthermore, our methodology allows us to elucidate the complex interactions among bubbles, crystallites, and surfaces under shear flow conditions. We demonstrated that bubbles strongly affect scaling performance and heat transfer. This has previously been prevented through degassed solutions,[48] which is impractical for large volumes of cooling water utilized in technical applications. We revealed and quantified the appearance, residence time, and bubble coverage dependent on the surface chemical composition and structure. We showed that the bubbles increase locally the temperature of the substrate, leading to hot spots and contact line effects, inducing heterogeneous temperature variations and evaporation, which promote the nucleation and growth of crystals. Through nanostructuring to reach superhydrophilicity, we were able to prevent the formation and growth of bubbles without significantly altering the nucleation behavior of calcium sulfate.

Our findings suggest that in cases where a surface experiences fouling induced by bubbles, the design of scalephobic surfaces should prioritize engineering the suppression of surface bubbles, without substantially affecting the free energy barrier to nucleation for the foulant. This is crucial because these bubbles, along with the forming contact line, constitute the primary enhancing mechanism of fouling. Direct optical access is crucial for investigating this type of fouling. Our research has demonstrated that the formation and dissolution effects associated with the presence of contact lines cannot be measured solely through fouling resistance assessments. We have not observed continuously occurring detachments of fouling with the tested flow conditions indicating that crystallite adhesion is stronger than bubble adhesion. We demonstrated the effectiveness of a nanostructured surface which shows reduced scale formation, one of the sought-after properties toward realizing intrinsically scalephobic surfaces.[33] Counterintuitively, the introduced nanostructure with its enlarged surface area did not adversely affect nucleation behavior of scale to a point of larger mass gains. Specifically, we showed that this surface can reduce the ex situ measured, area and time averaged mass gain by 3.5× compared to a superhydrophobic surface under the same shear flow conditions with an 82% higher heat transfer coefficient. The hydrophilic nanostructure surface unexpectedly prolonged the roughness control phase beyond the end of the experiment of the other three surfaces. This highlights the promising potential of nanostructured surfaces in addressing fouling. The results further demonstrate that the surface is effective at low flow velocities and low Reynolds numbers, where fouling is more pronounced.[39] Moreover, the scalephobic properties are expected to be even more effective at higher Reynolds numbers, where additional effects, such as fouling detachment,[10] enhance its performance. We anticipate that these findings can provide important information for the design of scalephobic surfaces and can also be relevant for other interfacial transport research areas.[69] Last, while our work focused on the nucleation and growth of crystallites, it opens opportunities for further work on investigating the entire fouling process, including removal mechanism, under heat transfer conditions and higher shear flow regimes, as would be present in technical applications.

4. Experimental Section

Materials: 1H,1H,2H,2H-perfluorodecyl acrylate (CAS No: 27905-45-9), trichlorovinylsilane (CAS No: 75-94-5), tert-butyl peroxide(CAS No: 110-05-4), $CaSO_4$ dihydrate(CAS No: 10101-41-4), phosphoric acid (CAS No: 7664-38-2), sodium chlorite (CAS No: 7758-19-2), sodium hydroxide (CAS No: 1310-73-2), sodium phosphate tribasic dodecahydrate (CAS No: 10101-89-0) all Sigma-Aldrich Merck, CU-DHP substrates (Conrad Electronic International GmbH & Co. KG), Kryonaut Extreme (Thermal Grizzly).

Surface Preparation: All tested surfaces were fabricated on 18 mm x 18 mm x 0.5 mm CU-DHP substrates k_{co} = 318 W m^{-1} K^{-1}). Before electropolishing, the substrates were mechanically polished by hand using 1200 grit wet sandpaper. After sonication in DI water for 5 min the substrates were dried with nitrogen. Subsequently, a conductive copper tape was attached to the back of the substrate, serving as a connection point for the anode cables to the power supply. It is essential that the copper tape maintains sole contact with the substrate, ensuring it is not in contact with the polishing solution. To achieve this, Kapton tape was employed to insulate the copper tape and the substrate's back surface, as only one side of the substrate undergoes polishing. For the electropolishing process, a solution comprised of phosphoric acid (H_3PO_4) and DI water in a 2:1 volume ratio was utilized. The cathode, possessing four times the surface area of the anode, consists of two additional rough copper samples exposed on both their front and back surfaces. The electrodes were positioned ≈4 cm apart within a 200 mL beaker. Finally, the process itself was current controlled by a power source at 3.55 A. The samples were polished in the solution for 5 min, followed by DI water rinsing and drying with nitrogen. All tested surfaces were stored in petri dishes to prevent contamination and were tested within

2 weeks of fabrication to ensure reliability and consistency. The surfaces maintain their contact angles (Table 2) for extended periods beyond the 2 weeks.

Nanostructuring: The previous electropolished substrates were cleaned using bath sonication separately in acetone, isopropyl alcohol, and DI water for 5 min each, followed by drying with nitrogen. For the nanostructuring synthesis, we used a previously published recipe[70] to prepare the etching solution. Subsequently, each sample was immersed in the etching solution maintained at a temperature of 95 °C for a duration of 5 min, followed by DI water rinsing and drying with nitrogen. The back of the substrates was again polished with 1200-grit sandpaper to remove the oxide layer.

pPFDA Fluoropolymer Coating: The process of grafting a polymer coating using initiated chemical vapor deposition (iCVD) was conducted in three sequential steps. The electropolished or nanostructured substrates were first placed in oxygen plasma for 5 min at 0.6 mbar (Femto, Diener electronic). Next, the substrates were transferred to a custom-made CVD chamber maintained at 80 mTorr to form a coating of trichlorovinylsilane (TCVS) for 20 min. Following the TCVS coating, an ultrathin layer of 1H,1H,2H,2H-perfluorodecyl acrylate (PFDA; 97% was deposited as a monomer, employing the iCVD tool (iLab Coating System, GVD Corporation). This deposition occurred in the presence of tert-butyl peroxide (98%) acting as an initiator. Throughout the process, the chamber pressure was regulated to ≈100 mTorr, with the base temperature set at 39 °C, and the filament temperature for monomer and initiator decomposition maintained at 300 °C. The duration of the coating process was 15 min for a 40 nm thic coating.[71]

Hard Water Preparation: The hard water for the crystallization experiments was prepared by dissolving previously ground $CaSO_4$ dihydrate in DI water (2 g L^{-1}). The solution was mixed for 1 h and consequently kept at 55 °C to evaporate ≈ 4 L of the solvent. To remove formed crystals, the solution was filtered using a MN 615 filter (Macherey-Nagel, retention capacity 4–12 µm).

Crystallization Fouling Experiments: The continuous flow fouling unit consisted of a membrane pump (Shurflo 8000- 543-290), which was connected in series to a flowmeter (BIOTECH, fch-m-pom; accuracy: ±2%), a home built parallel plate chamber, and a temperature-controlled reservoir. We applied for the crystallization tests flow rates of 0.35 L min^{-1}, resulting in flow velocity of $\bar{u} \approx 0.05$ m s^{-1} and $Re = \rho \bar{u} d_h / \mu \approx 440$ at the test section (height $l = 5$ mm x channel width $w = 25.1$ mm, $d_h = 2wl/(l+w) = 8.1$ mm. The heating zone consisted of an external powered heating cartridge (PROBAG HS 208), which was connected to an external power source, an intermediate copper block, and the sample to study. The adjustable heater cartridge maintained a sample dependent power level (±2%) throughout the experiment. We ensured uniform temperature distribution by attaching the embedded sample to an intermediate copper block, promoting consistent heat transfer. Thermal paste (Thermal Grizzly Kryonaut Extreme, $k_{paste} = 14.2$ W m^{-1} K^{-1}) enhanced conductivity and attachment between the sample and the copper rod. We used five previously calibrated thermocouples (T-Type, ±0.1 K, $d = 1$ mm) embedded in the copper block with axially uniform spacing to determine the heat flux $q'' = k\frac{\partial T}{\partial z}$ (±5%) using Fourier's law of conduction, which facilitated the determination of the sample temperature T_S by a linear extrapolation (Section S1, Supporting Information). We achieved the consistent T_S by adjusting P_{in} of the heating cartridge dependent on the surface type. We calculated h and R_f values at 0.05 Hz using Newton's law of cooling. We implemented two stop criteria for the experiments: either reaching $T_S = 98$ °C to prevent boiling or reaching the experimental time limit of $t = 10$ h.

We placed the flow fouling unit upside down in horizontal direction (Figure S1, Supporting Information) on a home-built microscope. We utilized a high-resolution CMOS camera (Grasshopper 3 GS3-U3-32S4M, FLIR) and a 4× objective lens (Plan N, Olympus) to perform and capture bright field microscopic images of the surface at the same acquisition rate. This approach allowed us to thoroughly analyze the visual details of bubbles and the fouling behavior over a large surface area. We obtained all sensor control and data acquisition using a data acquisition system (Beckhoff) and LabView.

Bubble Coverage Analysis: The projected area of bubbles in bright-field images for bubble coverage calculation was analyzed with a trained instance segmentation algorithm using Detectron2.[72] A total loss of 0.02581 was reached after 500 000 training steps with a training dataset labeled by us. The bounding box mean average precision is 93.9 and the segmentation mean average precision is 95.6.

Bubble Residence Time Analysis: The residence time of 15 individual bubbles were analyzed and averaged for each surface type. For the superhydrophobic surface we observed bubbles which covered the entire observable region for extended periods (>220 s) and values are not applicable.

Contact Angle Measurement: Surface wettability was assessed by measuring advancing and receding contact angles using an inflating and deflating water droplet, less than 8 µL, on a goniometer (OCA 35, Dataphysics). Five measurements were conducted at random locations for each surface. The air bubble contact angle measurements were performed on submerged substrates in DI water and HW on the same system.

Supporting Information

Supporting Information is available from the Wiley Online Library or from the author.

Acknowledgements

J.S. and T.A. contributed equally to this work. This work acknowledges the assistance of L. Steinmann, and P. Feusi (all from ETH Zurich) for technical support; C. Scheuer, A. Hugentobler, E. Gesatti, and M. Bischof for their spadework; A. Tripathy for his help using the iCVD system; MTSN staff, J. Armstrong, and K. Schmid for the fruitful discussions during the various stages of the research. Funding: This project has received funding from the European Research Council (ERC) under the European Union's Horizon 2020 research (DESCALE; Grant agreement No. 853257).

Conflict of Interest

The authors declare no conflict of interest.

Data Availability Statement

The data that support the findings of this study are openly available in the Eidgenössche Technische Hochschule Research Collection at https://doi.org/10.3929/ethz-b-000686330.

Keywords

crystallization fouling, heat transfer, nanostructures, scalephobicity, shear flow, surface engineering

Received: May 8, 2024
Revised: July 30, 2024
Published online: August 17, 2024

[1] J. Berce, M. Zupančič, M. Može, I. Golobič, *Processes* **2021**, *9*, 1356.
[2] H. Müller-Steinhagen, in *Advances in Heat Transfer*, Elsevier, Amsterdam **1999**.
[3] Z. Amjad, K. D. Demadis, *Mineral Scales and Deposits*, Elsevier, Amsterdam **2015**.

[4] D. M. Warsinger, J. Swaminathan, E. Guillen-Burrieza, H. A. Arafat, J. H. Lienhard V, *Desalination* **2015**, *356*, 294.
[5] J. Zhao, M. Wang, H. M. S. Lababidi, H. Al-Adwani, K. K. Gleason, *Desalination* **2018**, *442*, 75.
[6] J. J. Urban, *Joule*. **2017**, *1*, 665.
[7] M. R. Malayeri, A. Al-Janabi, H. Müller-Steinhagen, *Int. J. Energy Res.* **2009**, *33*, 1101.
[8] A. Goswami, S. C. Pillai, G. McGranaghan, *Chem. Eng. J. Adv.* **2023**, *16*, 100519.
[9] J. Meng, S. Wang, *Adv. Funct. Mater.* **2020**, *30*, 1904796.
[10] J. Schmid, T. Armstrong, F. J. Dickhardt, S. R. Iqbal, T. M. Schutzius, *Sci. Adv.* **2023**, *9*, eadj0324.
[11] A. Herz, M. R. Malayeri, H. Müller-Steinhagen, *Energy Convers. Manage.* **2008**, *49*, 3381.
[12] M. Bohnet, *Chem. Eng. Technol.* **2003**, *26*, 1055.
[13] V. Eroini, N. Kapur, A. Neville, M. Euvrard, CORROSION 2011, (March 2011).
[14] M. Izadi, D. K. Aidun, P. Marzocca, H. Lee, in *Fluid Flow, Heat Transfer and Thermal Systems, Parts A and B*, ASMEDC, NY **2010**.
[15] W. C. Cheong, P. H. Gaskell, A. Neville, *J. Cryst. Growth*. **2013**, *363*, 7.
[16] A. Quddus, L. M. Al-Hadhrami, *J. Thermophys. Heat Transfer.* **2011**, *25*, 112.
[17] M. Alahmad, *Chem. Eng. Technol.* **2008**, *31*, 149.
[18] H.-Q. Jin, H. Athreya, S. Wang, K. Nawaz, *Desalination*. **2022**, *532*, 115754.
[19] R. Zhang, G. Azimi, *ACS Appl. Mater. Interfaces*. **2020**, *12*, 42339.
[20] G. Azimi, Y. Cui, A. Sabanska, K. K. Varanasi, *Appl. Surf. Sci.* **2014**, *313*, 591.
[21] Q. Zhao, Y. Liu, *Appl. Surf. Sci.* **2004**, *229*, 56.
[22] M. Förster, W. Augustin, M. Bohnet, *Chem Eng Process.* **1999**, *38*, 449.
[23] Y. Cai, M. Liu, L. Hui, *Ind. Eng. Chem. Res.* **2014**, *53*, 3509.
[24] H. Müller-Steinhagen, Q. Zhao, *Chem. Eng. Sci.* **1997**, *52*, 3321.
[25] S. A. McBride, H.-L. Girard, K. K. Varanasi, *Sci. Adv.* **2021**, *7*, abe6960.
[26] W. Jiang, J. He, F. Xiao, S. Yuan, H. Lu, B. Liang, *Ind. Eng. Chem. Res.* **2015**, *54*, 6874.
[27] T. Zhang, Y. Wang, F. Zhang, X. Chen, G. Hu, J. Meng, S. Wang, *NPG Asia Mater.* **2018**, *10*, e471.
[28] T. V. J. Charpentier, A. Neville, S. Baudin, M. J. Smith, M. Euvrard, A. Bell, C. Wang, R. Barker, *J. Colloid Interface Sci.* **2015**, *444*, 81.
[29] S. B. Subramanyam, G. Azimi, K. K. Varanasi, *Adv. Mater. Interfaces.* **2014**, *1*, 1300068.
[30] M. F. B. Sousa, G. F. Barbosa, F. Signorelli, C. A. Bertran, *Surf. Coat. Technol.* **2017**, *325*, 58.
[31] M. F. B. Sousa, H. C. Loureiro, C. A. Bertran, *Surf. Coat. Technol.* **2020**, *382*, 125160.
[32] X. Yao, W. Lin, M. Wang, S. Wang, *Small*. **2022**, *18*, 2203615.
[33] Y. Wang, J. Meng, S. Wang, *Langmuir*. **2021**, *37*, 8639.
[34] M. J. Kreder, D. Daniel, A. Tetreault, Z. Cao, B. Lemaire, J. V. I. Timonen, J. Aizenberg, *Phys. Rev. X*. **2018**, *8*, 031053.
[35] Y. Liu, J. S. Wexler, C. Schönecker, H. A. Stone, *Phys. Rev. E: Stat. Phys., Plasmas, Fluids, Relat. Interdiscip. Top.* **2016**, *1*, 074003.
[36] L. M. Hamm, A. J. Giuffre, N. Han, J. Tao, D. Wang, J. J. De Yoreo, P. M. Dove, *Proc Natl Acad Sci USA*. **2014**, *111*, 1304.
[37] S. Hatte, R. Pitchumani, *Ind. Eng. Chem. Res.* **2022**, *61*, 14355.
[38] B. Bansal, H. Müller-Steinhagen, *J. Heat Transfer* **1993**, *115*, 584.
[39] L.-C. Wang, S.-F. Li, L.-B. Wang, K. Cui, Q.-L. Zhang, H.-B. Liu, G. Li, *Exp. Therm. Fluid Sci.* **2016**, *74*, 143.
[40] A. Al-Gailani, O. Sanni, T. V. J. Charpentier, R. Crisp, J. H. Bruins, A. Neville, *Appl. Therm. Eng.* **2021**, *184*, 116271.
[41] W. Ma, Z. Wang, F. Jiao, Y. Zhen, C. Ma, *Environ. Prog. Sustainable Energy*. **2019**, *38*, 13163.
[42] H. Zhao, S. Khodakarami, C. A. Deshpande, J. Ma, Q. Wu, S. Sett, N. Miljkovic, *ACS Appl. Mater. Interfaces* **2021**, *13*, 38666.
[43] W. Tae Kim, C. Bai, Y. I. Cho, *Int. J. Heat Mass Transf.* **2002**, *45*, 597.
[44] O. Sanni, O. Bukuaghangin, M. Huggan, N. Kapur, T. Charpentier, A. Neville, *Rev. Sci. Instrum.* **2017**, *88*, 103903.
[45] S. F. Jones, G. M. Evans, K. P. Galvin, *Adv. Colloid Interface Sci.* **1999**, *80*, 27.
[46] R. Battino, T. R. Rettich, T. Tominaga, *J. Phys. Chem. Ref. Data.* **1984**, *13*, 563.
[47] T. Huppertz, H. Nieuwenhuijse, *Int. Dairy J.* **2022**, *126*, 105236.
[48] H. Kiepfer, P. Stannek, M. Kuypers, M. Grundler, H. J. Bart, *Heat Mass Transfer.* **2023**, *60*, 785.
[49] X. Wang, S. Zhao, H. Wang, T. Pan, *Appl. Therm. Eng.* **2012**, *35*, 112.
[50] S. Dash, L. Rapoport, K. K. Varanasi, *Langmuir.* **2018**, *34*, 782.
[51] M. E. O'Neill, *Chem. Eng. Sci.* **1968**, *23*, 1293.
[52] T. Petrova, R. B. Dooley, *Proc. Int. Assoc. Prop. Water Steam* **2014**, *63*, 23.
[53] J. F. Klausner, R. Mei, D. M. Bernhard, L. Z. Zeng, *Int J Heat Mass Transf.* **1993**, *36*, 651.
[54] G. B. Darband, M. Aliofkhazraei, S. Shanmugam, *Renew Sustain Energy Rev.* **2019**, *114*, 109300.
[55] J. E. George, S. Chidangil, S. D. George, *Adv. Mater. Interfaces.* **2017**, *4*, 1601088.
[56] D. Jeon, J. Park, C. Shin, H. Kim, J.-W. Jang, D. W. Lee, J. Ryu, *Sci. Adv.* **2020**, *6*, eaaz3944.
[57] J. Park, D. Jeon, Y. Kang, J. Ryu, D. W. Lee, *J. Mater. Chem. A.* **2023**, *11*, 1658.
[58] Y. Kang, S. Lee, S. Han, D. Jeon, M. Bae, Y. Choi, D. W. Lee, J. Ryu, *Adv. Funct. Mater.* **2024**, *34*, 2308827.
[59] Z. Lu, W. Zhu, X. Yu, H. Zhang, Y. Li, X. Sun, X. Wang, H. Wang, J. Wang, J. Luo, X. Lei, L. Jiang, *Adv. Mater.* **2014**, *26*, 2683.
[60] J. Ryu, D. W. Lee, *J. Mater. Chem. A.* **2024**, *12*, 10012.
[61] T. Cebeci, P. Bradshaw, *Physical and Computational Aspects of Convective Heat Transfer*, Springer New York, NY **1988**.
[62] A. Cowley, D. Maynes, J. Crockett, B. D. Iverson, *Int J Heat Mass Transf.* **2018**, *121*, 196.
[63] F. Albert, W. Augustin, S. Scholl, *Chem. Eng. Sci.* **2011**, *66*, 499.
[64] N. Shahidzadeh-Bonn, S. Rafaï, D. Bonn, G. Wegdam, *Langmuir.* **2008**, *24*, 8599.
[65] D. Fairhurst, in *Droplet Wetting and Evaporation*, Elsevier, Amsterdam **2015**.
[66] R. P. Sear, *Int. Mater. Rev.* **2012**, *57*, 328.
[67] K. Zuo, X. Zhang, X. Huang, E. F. Oliveira, H. Guo, T. Zhai, W. Wang, P. J. J. Alvarez, M. Elimelech, P. M. Ajayan, J. Lou, Q. Li, *Nat. Commun.* **2022**, *13*, 4523.
[68] C. Walker, S. Lerch, M. Reininger, H. Eghlidi, A. Milionis, T. M. Schutzius, D. Poulikakos, *ACS Nano.* **2018**, *12*, 8288.
[69] J. Berce, K. Arhar, A. Hadžić, M. Zupančič, M. Može, I. Golobič, *Appl. Therm. Eng.* **2024**, *242*, 122540.
[70] R. Enright, N. Miljkovic, N. Dou, Y. Nam, E. N. Wang, *J Heat Transfer.* **2013**, *135*, 091304.
[71] A. Tripathy, K. Regulagadda, C. W. E. Lam, M. A. Donati, A. Milionis, C. S. Sharma, E. Mitridis, T. M. Schutzius, D. Poulikakos, *Langmuir.* **2022**, *38*, 11296.
[72] Y. Wu, A. Kirillov, F. Massa, W.-Y. Lo, R. Girshick, "Detectron2", https://github.com/facebookresearch/detectron2, accessed: July, **2019**.